J|A|C|S

JOURNAL OF THE AMERICAN CHEMICAL SOCIETY

Atomic Resolution Observation of a Size-Dependent Change in the Ripening Modes of Mass-Selected Au Nanoclusters Involved in CO Oxidation
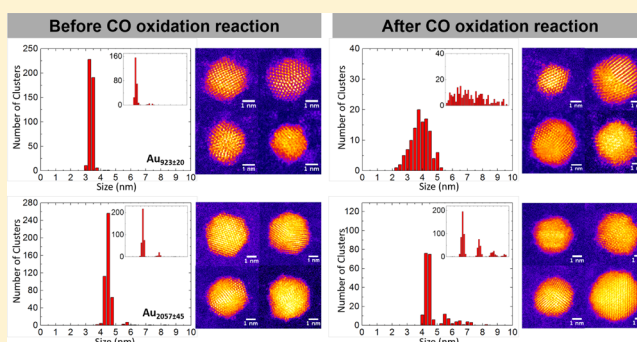
Kuo-Juei Hu,[†] Simon R. Plant,[†] Peter R. Ellis,[‡] Christopher M. Brown,[‡] Peter T. Bishop,[‡] and Richard E. Palmer[*,†]

[†]Nanoscale Physics Research Laboratory, School of Physics and Astronomy, University of Birmingham, Birmingham, B15 2TT, U.K.
[‡]Johnson Matthey Technology Centre, Blounts Court Road, Sonning Common, Reading, RG4 9NH, U.K.

S *Supporting Information*

ABSTRACT: Identifying the ripening modes of supported metal nanoparticles used in heterogeneous catalysis can provide important insights into the mechanisms that lead to sintering. We report the observation of a crossover from Smoluchowski to Ostwald ripening, under realistic reaction conditions, for monomodal populations of precisely defined gold particles in the nanometer size range, as a function of decreasing particle size. We study the effects of the CO oxidation reaction on the size distributions and atomic structures of mass-selected $Au_{561\pm13}$, $Au_{923\pm20}$ and $Au_{2057\pm45}$ clusters supported on amorphous carbon films. Under the same conditions, $Au_{561\pm13}$ and $Au_{923\pm20}$ clusters are found to exhibit Ostwald ripening, whereas $Au_{2057\pm45}$ ripens through cluster diffusion and coalescence only (Smoluchowski ripening). The Ostwald ripening is not activated by thermal annealing or heating in O_2 alone.
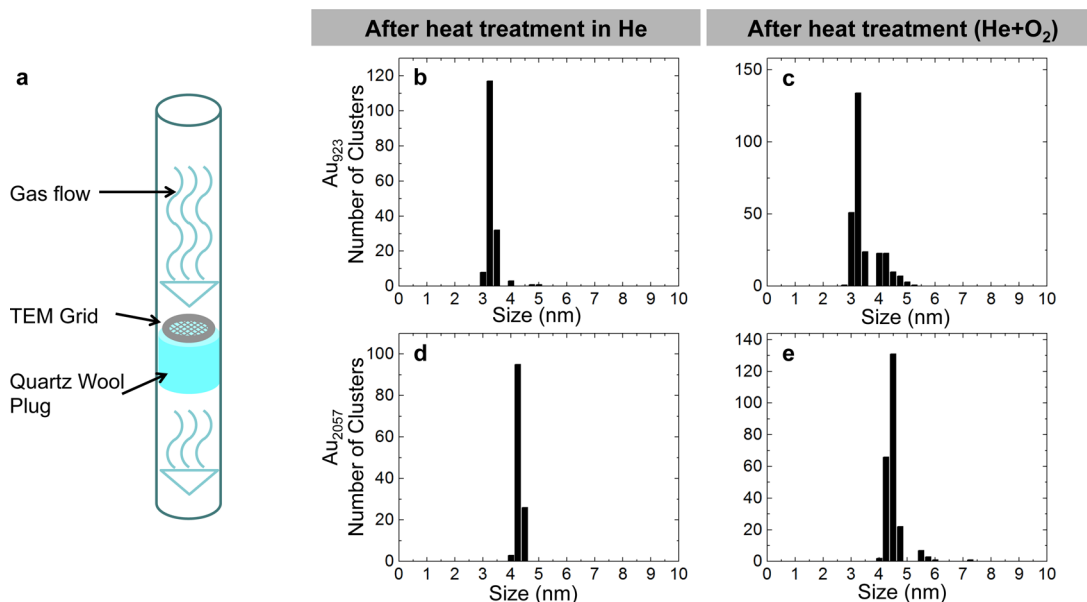
INTRODUCTION

The inhibition of sintering remains a central challenge for heterogeneous catalysis using ultrafine metal particles.[1,2] Sintering leads to the coarsening of the particles, and hence the irreversible deactivation of their catalytic activity as the average particle size increases over time.[3] This places limitations on the efficiency and longevity of supported metal particle catalysts. The size and morphology of small catalyst particles is integral to their activity, as these parameters determine the number of active sites (e.g., facet and edge sites), and other size-dependent electronic and quantum effects.[4] Particle ripening is commonly ascribed to one of two modes: *Ostwald ripening,*[5,6] in which large particles grow at the expense of smaller particles through the migration of single atoms or small atomic clusters, and *Smoluchowski ripening,*[7] in which whole particles are free to diffuse and coalesce with neighboring particles. Nanoparticle ripening modes have been investigated in situ with environmental TEM;[8−11] however, the challenge is to replicate realistic reaction conditions while also decoupling the effects of any damage induced through exposure to the electron beam. In general, the imaging of small clusters at the atomic level, even in vacuo, remains challenging.[4,12] It has long been known that supported metal clusters exhibit size-dependent catalytic properties,[13] although it has only been recently that catalytically active, size-selected Pt_N (N = 22, 68) clusters on oxide supports have been used to provide evidence of Ostwald ripening suppression in truly monomodal populations.[14] Particle size has long been associated with catalyst sintering kinetics,[15] but detailed studies of truly monodisperse nanoparticles at atomic resolution have proved elusive.

Using amorphous carbon supports in the present work, we begin with stable populations of monodisperse, mass-selected particles centered at the magic number sizes of Au_N (N = 561, 923, 2057). Au nanoparticles of this size range are found to be active in catalyzing CO oxidation,[4,16−21] at low temperatures (≥273 K) in particular.[17] Indeed, heterogeneous catalysis using Au nanoparticles or clusters (<5 nm in size) has been studied extensively on a variety of supports (e.g., oxides, carbons, polymers), both for gas- and liquid-phase reactions.[16,18,22−24] Au on carbon presents a versatile selective oxidation catalyst for a number of reactions.[25] Although generally the catalytic activity of Au/C is considered to be low for CO oxidation below ambient temperature, an important example is CO oxidation at RT using highly dispersed (2−5 nm) Au particles supported on activated carbon fibers.[26] Commonly, Au particles catalyzing CO oxidation at low temperature are supported on transition metal oxides, however, HAADF-STEM studies reveal that Au particles in the size range relevant to the present work

Figure 1. (a) Schematic diagram illustrating the gas-flow reaction setup for the treatment of mass-selected Au nanoclusters supported on amorphous carbon. (b−e) Histograms showing the size distributions for (b,c) $Au_{923\pm20}$ and (d,e) $Au_{2057\pm45}$ following (b,d) heat treatment in a pure He atmosphere (0.35 bar at 250 °C) and (c,e) after the introduction of O_2 (concentration by volume: 20.9% O_2, 79.1% He), with the pressure initially at 0.10 bar rising to 0.14 bar ($Au_{923\pm20}$) and 0.12 bar ($Au_{2057\pm45}$) at 250 °C.

(2−3 nm) exhibit semicoherent interfacial expitaxy,[27,28] meaning that the morphology of the particles is, broadly, quasi-hemispehrical, rather than quasi-spherical, as for free-standing clusters.

The interest in magic numbers stems from theoretical treatments that indicate abrupt variations in the adsorption energies, e.g., for oxygen and CO, on Au clusters at magic number sizes.[29,30] Low coordinated atoms at edge and corner sites may play a role in the catalytic activity of gold clusters and nanoparticles[31] and, for small clusters mimicking corner sites of larger (2−5 nm) particles, gold is predicted to be more catalytically active toward CO oxidation than other transition and noble metals.[32] Au can effectively catalyze the reaction even for few-atom particles.[33,34] The study of Au catalysts by UHV-STM, for instance Au on titania,[35] has elucidated the sintering kinetics, suggesting that sintering is reaction-induced. There is much still to explore experimentally using accurately mass-selected clusters as model systems to complement the theory. Indeed, there is renewed interest in predictions of the relative stabilities for the geometric, magic-number high-symmetry isomers (I_h, D_{5h}, O_h) of Au nanoclusters with sizes up to 3.5 nm,[36] prompted in particular by the recent experimental demonstration of atomic structure control for Au_{923} in the cluster beam source.[37]
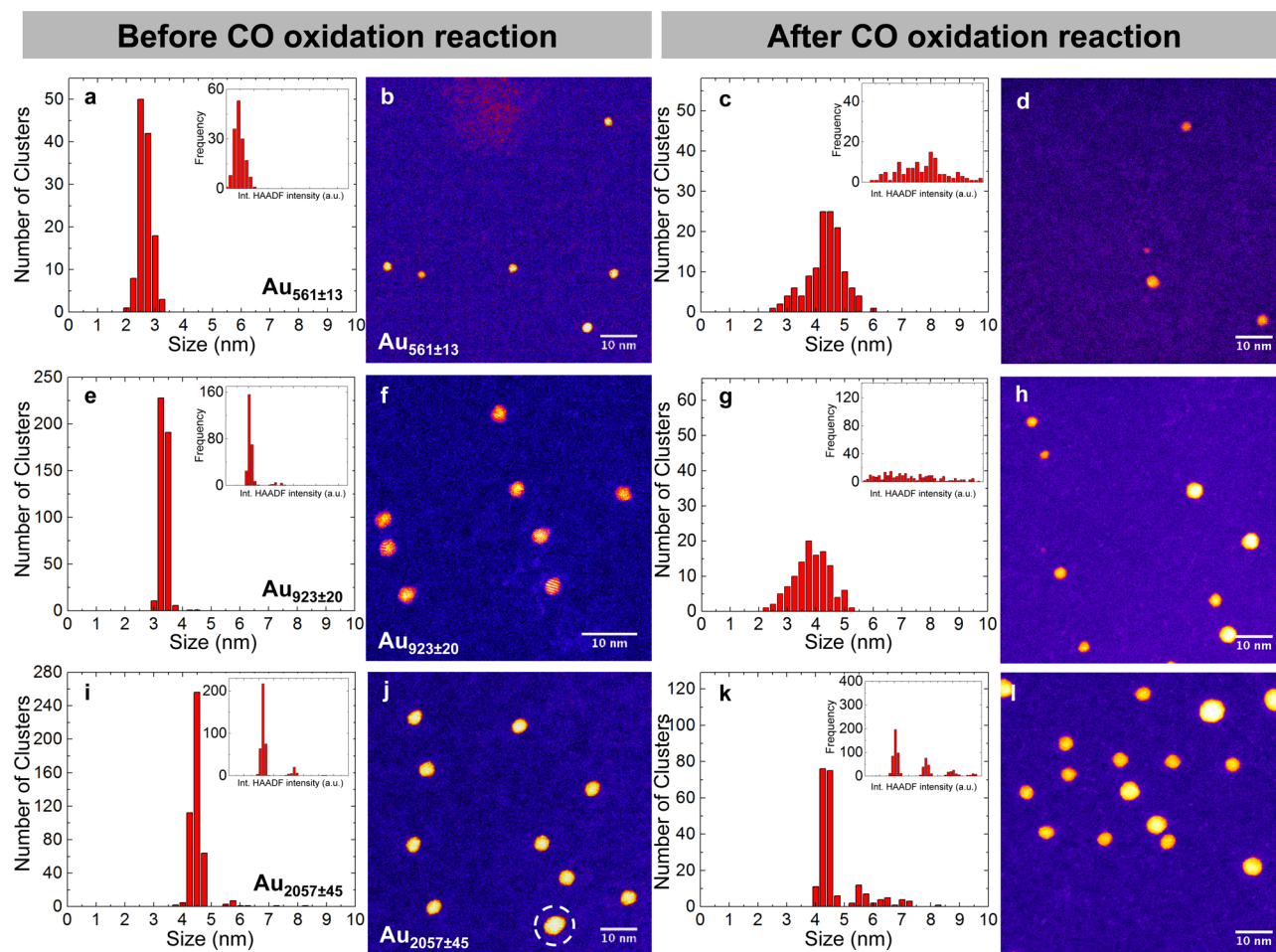
Here, by using monomodal populations of atomically precise particles in the nanometer size range, we reveal the crossover between Ostwald and Smoluchowski ripening modes, as a function of particle size, and under realistic reaction conditions. We investigate the effect of CO oxidation reaction conditions (0.15 ± 0.1 bar, 250 °C) on the size and atomic structures of mass-selected $Au_{561\pm13}$, $Au_{923\pm20}$ and $Au_{2057\pm45}$ clusters supported on amorphous carbon films. We find that $Au_{561\pm13}$ and $Au_{923\pm20}$ clusters exhibit Ostwald ripening, whereas $Au_{2057\pm45}$ ripens through coalescence and diffusion only. Indeed, what we show may account for the perceived preferential disappearance of certain particle sizes during sintering.[10] Furthermore, we determine for $Au_{923\pm20}$ that

Ostwald ripening is activated by the combustion of CO, and not by thermal annealing (0.35 bar, 250 °C) nor the presence of O_2 alone (0.14 bar ($Au_{923\pm20}$) and 0.12 bar ($Au_{2057\pm45}$) at 250 °C).

RESULTS AND DISCUSSION

Populations of mass-selected clusters exhibit very narrow particle size distributions that are approximately Gaussian (see as examples Figure 1(b,d) and Figure 2(a,e,i)). This is advantageous given that Granqvist and Buhrman posited that the ripening mode could be identified simply by the weighting (skewness) of the particle size distribution.[7] Historically, the challenge to verify the Granqvist−Buhrman phenomenon experimentally has been 2-fold: to track the change in the particle size distribution given that supported nanoparticles tend to exhibit an inherent broad, log-normal distribution from the outset, and to perform the analysis at the single particle level while amassing meaningful statistics. Mass-selected clusters can provide a valuable insight into the ripening process,[14] as there are no clusters smaller than the original, predetermined size to be consumed in favor of other sizes. Clusters that result from ripening are therefore highly distinguishable from the original clusters. Furthermore, a monomodal population of clusters implies the same cohesive energy for all particles, and therefore the same energy required to liberate atoms and undergo fragmentation for all particles within the sample population.

Our aim is to preserve the free-space properties (size and structure) at the point of deposition onto a support. Of course, morphology is substrate-dependent,[38] and carbon supports offer advantages in this regard: the weak interactions between carbon and small metal particles has long been established,[39] and thus the supported particles retain the quasi-sphericity of their free space structures under soft-landing conditions (energy per cluster, 0.5 eV). Yet the clusters are not freely mobile on amorphous carbon:[40,41] they are sufficiently stable on the surface to remain monodisperse at room temperature, in
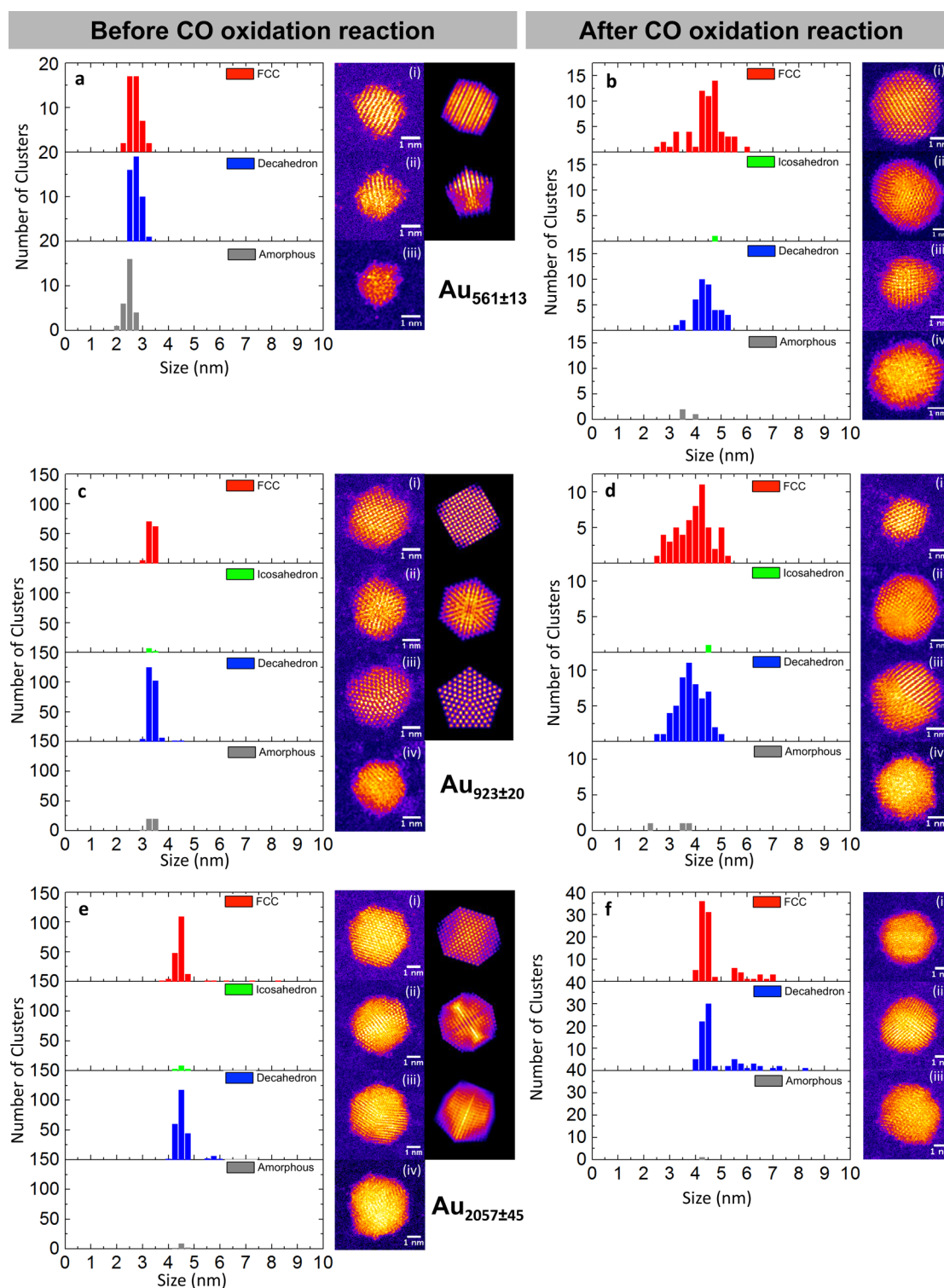
Figure 2. Histograms of the particle size distributions for mass-selected $Au_{561\pm13}$, $Au_{923\pm20}$ and $Au_{2057\pm45}$ nanoclusters both before (a,e,i) and after (c,g,k) exposure to the CO oxidation reaction conditions. The integrated HAADF-STEM intensity distributions are shown inset; the areas for the pair in each row have been normalized to enable comparison. The distributions are accompanied by representative HAADF-STEM images before (b,f,j) and after (d,h,l) the reaction. Conditions of the CO oxidation reaction: 0.15 ± 0.1 bar, 250 °C (ramp rate of 2 °C min^{-1} from RT and dwell for 2 h). Gas mixture by volume: 1% CO + 20.9% O_2 + 78.1% He.

common with the behavior observed on graphene[42] and graphene oxide.[43] This differs from the case of graphite, for which both Ag and Au clusters diffuse across the atomically flat terraces at RT,[44,45] unless energetically pinned,[46,47] in which case, depending on size and binding energy, the clusters may resist lateral diffusion up to several hundred degrees above RT, undergoing Ostwald ripening above a threshold temperature.[48] Size-selected clusters pinned in this manner have been shown to resist sintering under realistic reaction conditions.[49] An additional virtue of using carbon as the support is that the atomic number is sufficiently low to offer high contrast imaging in HAADF-STEM, as the relative intensity (I_R) of gold to carbon in the image follows the relationship, $I_R = I_{Au}/I_C = (N_{Au}/N_C)(Z_{Au}/Z_C)^{\alpha}$, where N represents the number of atoms and $\alpha = 1.46 \pm 0.18$ is an instrument-specific parameter, which has been calibrated previously at an inner collection angle of 62 mrad.[50] Given also that $I_{Au} \propto N_{Au}$, the relative masses of the particles can be determined quantitatively. Thus, the diameters of the particles can be measured directly from the HAADF-STEM images taken at atomic resolution, while the HAADF-STEM intensity distributions at lower magnification yield the relative particle masses within a given population. Evidence to demonstrate the resilience of the Au clusters (over a full range

of sizes) under the electron beam conditions used in the present study are provided in the Supporting Information.

In order to gain insights into the ripening mechanisms, we first seek to determine the effects due to separate thermal and O_2 treatments on the particle size distributions of $Au_{923\pm20}$ and $Au_{2057\pm45}$. Figure 1(a) shows a schematic representation of the gas-flow reaction setup for the treatment of mass-selected Au nanoclusters supported on amorphous carbon used for these treatments. Figure 1(b) and (d) reveal the results of the thermal treatment (250 °C) of $Au_{923\pm20}$ and $Au_{2057\pm45}$, during which the particles were protected under an inert, dynamic atmosphere of pure He. There is no shift in, nor broadening of, the discrete particle size distributions at the initial particle size, although there is some evidence of aggregation for $Au_{923\pm20}$ given the presence of a proportion of larger particles, although it is limited. By comparison, the introduction of O_2 into the dynamic atmosphere for a separate set of $Au_{923\pm20}$ and $Au_{2057\pm45}$ samples induces a more pronounced change in the particles' size distributions (Figure 1(c) and (e)), which, as it appears to be quantized, is consistent with enhancement of the rate of dimerization, which is more pronounced for $Au_{923\pm20}$ than for $Au_{2057\pm45}$. Thus, this behavior of whole particle migration and coalescence observed due to O_2 treatment is commensurate with Smoluchowski ripening. It is worth considering the factors

Figure 3. Histograms showing the size distributions as a function of the atomic structures for mass-selected $Au_{561\pm13}$, $Au_{923\pm20}$ and $Au_{2057\pm45}$ nanoclusters, both before (a,c,e) and after (b,d,f) exposure to the CO oxidation reaction conditions. Representative atomic resolution HAADF-STEM images are shown alongside (labeled i−iv, as appropriate), accompanied by multislice image simulations for the sizes Au_N (N = 561, 923, 2057).

that drive first surface diffusion then ripening of the particles: ambient temperature and the exothermicity of reaction. These factors then compete with the binding of the particles to defects, which governs the mean diffusion lengths. Of course, molecular oxygen at elevated temperatures can bind to surface defects to further attenuate interactions between particles and the support. Thus, clusters can be released from their original binding sites at the surface, allowing greater mobility.

Next, the behavior due to O_2 treatment is contrasted with the effects of the CO oxidation reaction. The panel shown in Figure 2 illustrates the transformation in the particle sizes for $Au_{561\pm13}$, $Au_{923\pm20}$ and $Au_{2057\pm45}$. The corresponding and representative

HAADF-STEM images (Figure 2(b,f,j)) taken before reaction, reveal the randomly distributed, monodispersed particles, the general morphology of which is quasispherical, as expected. Specifically, Figure 2(a,e,i) presents the original particle size distributions for each of these mass-selected Au clusters, with the integrated HAADF intensity distributions shown inset. The diameter distribution for mass-selected $Au_{561\pm13}$ (Figure 2(a)) exhibits a mean diameter of 2.63 nm with a full-width half-maximum (fwhm) of 0.53 nm, which then transforms to a broad continuous distribution ranging between ∼2.5 and 6 nm following CO oxidation. A broadened, continuous distribution shifted to larger sizes, with almost no overlap of the original distribution, indicates Ostwald ripening. The trend is confirmed through the integrated HAADF intensity which is proportional to the number of atoms within each cluster, shown in inset of Figure 2(c), revealing a very scattered distribution. Similarly, the original diameter distribution for $Au_{923\pm20}$ is narrow with a peak centered at 3.36 nm and a fwhm of 0.32 nm (3.36 ± 0.16 nm). However, after the reaction, the distribution becomes very broad, ranging from circa 2 to 5.5 nm (see Figure 2(g)), which is also suggestive of Ostwald ripening, given that the distribution again shifts to larger sizes as compared to the original peak position. That is to say, the presence of clusters smaller than the original size indicates fragmentation accompanied by the growth of larger clusters.

A comparison of the insets in Figure 2(c) and (g) demonstrates that the number of atoms within each cluster changes from being centered at a specific mass to a broad mass range. Notably, for $Au_{923\pm20}$, no clusters were found to be <3 nm before reaction, whereas after the reaction, there are considerable quantities of clusters that are found to be smaller than the original particle size.

The effects of CO oxidation on $Au_{2057\pm45}$, shown in Figure 2(k), are in stark contrast with those for $Au_{561\pm13}$ and $Au_{923\pm20}$. The size distribution of $Au_{2057\pm45}$ clusters before reaction in Figure 2(i) has a very sharp peak centered at 4.41 ± 0.17 nm. A small number of clusters are found to be 5.70 ± 0.15 nm nm in diameter, which we attribute to spontaneous dimerization. Indeed, we note the presence of a dimer (denoted with a dashed circle) in the corresponding HAADF-STEM image shown in Figure 2(j), a feature that can occur either at source due to the deposition of a small fraction of doubly charged ($2m/2z$) particles, or through coalescence of coincident and proximate particles at the substrate. Figure 2(k) shows that, after the CO oxidation reaction, the size distribution of $Au_{2057\pm45}$ is different from that observed for both $Au_{561\pm13}$ and $Au_{923\pm20}$ after reaction, in that no clusters smaller than the initial size are observed and also aggregation is evident from the emergence of features larger than ∼5.5 nm. However, these new features are distributed in a discrete manner, instead of forming one broad, continuous distribution across a wide range of sizes as in Figure 2(c) and Figure 2(g). The Gaussian fitting of these features reveals peaks at 4.37 ± 0.17, 5.56 ± 0.17 and 6.39 ± 0.22 nm (Figure 2(k)), which we attribute to monomers, dimers and trimers, respectively. The trend is echoed, if not more pronounced, in the histogram of the integrated HAADF intensity, shown in the inset of Figure 2(k), revealing discrete peaks at regular intervals, directly corresponding to the quantization in terms of the number of atoms per particle. At 5.56 and 6.39 nm, the diameters of the dimers and trimers are 1.25 and 1.45 times the diameter of the original monomer, respectively. This supports a quasi-spherical model for these clusters, given that the volume increases with the cube

of the radius. The results are consistent with the diffusion and coalescence of whole clusters, such that Smoluchowski ripening is the mode of particle coarsening in this case. It is worth noting that reactivity starts to decrease when the diameter exceeds 4 nm.[4,16−21]

Previous studies have indicated that the ripening process can be triggered by CO oxidation, as in the present work.[35,51] Among them, control experiments were conducted to show that Ostwald ripening, under some controlled conditions, can only be seen when the Au clusters are exposed to a mixture of CO and oxygen, and that the presence of CO[35] alone would not activate the Ostwald ripening process. Several studies have shown that Au clusters at ∼3.5 nm in diameter exhibit the highest throughput in CO combustion.[18,19,51] A mechanism has been proposed that involves each CO combustion event releasing as much as 2.9 eV,[35,52−54] in which the liberated energy can induce hot electrons to activate fragmentation,[53−55] on top of the heating provided by the system. There is also evidence showing the possibility of atomic migration between clusters mediated by CO through the formation of volatile gold complexes.[16,56,57] Furthermore, a thorough modeling study reveals the possibility of promoting Ostwald ripening by CO-metal complexation by lowering the surface energy, and thus increasing the probability of disintegration.[58]

To further investigate the morphological transformations of the clusters due to the CO oxidation reaction, we examined the particles in HAADF-STEM at atomic resolution. This technique allows the full three-dimensional atomic structure of the particles to be resolved.[59] The magic-number gold clusters exhibit motifs that correspond to one of three high-symmetry, ordered structures, namely icosahedral (Ih), decahedral (Dh) and face-centered cubic (FCC). We are able to assign the particles according to their structural motifs by reference to a simulation atlas, one for each particle size of Au_{561}, Au_{923} and Au_{2057}, each of which contains a series of multislice HAADF-STEM simulations generated over a full range of viewing orientations. (See the Supporting Information for simulation atlases.) We note that the particles may exhibit inherent surface reconstructions, an example being partially reconstructed decahedra observed for Au_{923} previously,[37,60] as well as the mobility of surface adatoms under the electron beam,[61] both of which are examples of deviations from the ideal case. Additionally, we often find there are a number of particles within a sample population that cannot be assigned to the ordered structures considered, and therefore we assign these particles as being amorphous or unidentified.

Figure 3 shows the particle size distributions "fractionated" according to atomic structure, both before and after the CO oxidation reaction. These diameter distributions therefore provide quantitative analyses of the high symmetry structures as a function of particle size. It is worth remarking that the proportions of Ih isomers in all sample populations are low (≤3%). Also, only the $Au_{561\pm13}$ sample population (Figure 3(a)) exhibits any significant proportion of amorphous structures (22%), and the number of amorphous particles observed for that sample population actually diminishes to ∼2% following CO oxidation (Figure 3(b)). Indeed, it is clear from the distributions shown in Figure 3 that the CO oxidation reaction does not cause amorphization of the particles. The results are entirely consistent with previous experimental evidence that Ih is metastable with respect to Dh and FCC,[37,60] and further that annealing leads to FCC specifically for Au_{561}.[62]

For $Au_{923\pm20}$, atomic resolution images taken after reaction (Figure 3(d)) reveal particles smaller than the original cluster size, as well as significantly enlarged clusters that are the result of Ostwald ripening. All particles are observed to maintain high symmetry configurations, and possess a quasi-spherical morphology. The proportion of decahedral to FCC structures was approximately 2:1 before reaction (Figure 3(c)) and became 1:1 after exposure to the CO oxidation reaction conditions (Figure 3(d)).

The proportions of Dh and FCC isomers of Au_{2057} that are monodisperse after reaction do change (comparing Figures 3(e) and (f)); however, we must also consider the atomic structure of clusters that aggregate to form dimers, trimers and tetramers (Figure 3(f)). If the isomers in a collision event are different, there is an ensuing competition then to adopt the most energetically favorable structure, although given that the relative surface energies of FCC and Dh structures are predicted to be similar in the size range 2000−6000 atoms,[63] the resulting statistical proportions of the isomers are expected to be approximately equivalent. We find that, overall, the ratio of FCC to Dh isomers before the reaction is in the approximate ratio of 3:4, whereas there is a slightly higher proportion (11:10 in the range of the monomer) of FCC to Dh clusters observed after reaction. In the size regime of the monomer, the proportion of FCC increases after reaction directly corresponding to a reduction in Dh isomers. We note that there were almost no Ih isomers and amorphous particles observed for $Au_{2057\pm45}$, both before and after the CO oxidation reaction.

Overall, the most intriguing phenomenon we have observed is that the extensive Ostwald ripening of $Au_{561\pm13}$ and $Au_{923\pm20}$ does not occur for $Au_{2057\pm45}$ under identical temperature and reaction conditions. Moreover, Ostwald ripening is not the mechanism for particle coarsening in the absence of 1% of CO, as the control experiments for $Au_{923\pm20}$ show, but instead ripening proceeds by diffusion and coalescence. It is therefore reasonable to conclude that the Ostwald ripening is driven by the chemical reaction itself, which may be due to a combination of the energy released from the exothermic reaction and the formation of metal complexes, which thus drives the liberation of atoms from the Au clusters. Given that catalytic activity also varies as a function of cluster size, the energy liberated can also vary. For instance, a cluster of diameter 3.5 nm (close to $Au_{923\pm20}$) is more active than that of 4.5 nm in diameter (close to $Au_{2057\pm45}$).[51] Surface free energy also rises with increasing cluster size.[64] At size $Au_{2057\pm45}$, the energy gained is not enough to drive atoms to detach from the clusters, so Ostwald ripening is prevented and only Smoluchowski ripening is possible. Although originating from different cluster sizes before ripening under exposure to the reaction conditions, it can be seen that for $Au_{561\pm13}$ and $Au_{923\pm20}$, both cases result in a broad distribution between 2.75 and 5.75 nm. Given the conclusion that these clusters undergo Ostwald ripening, once the cluster has grown to the limit such that Ostwald ripening should cease, clusters would not be able to grow bigger, but should instead reach a ceiling at this size.[64−68] Further growth would depend on the cluster diffusion around this ceiling size of 5.75 nm, which would depend in turn on the mean free path. We also suggest that clusters of size around 6 nm ($Au_{2057\pm45}$ dimer) are not highly mobile under the reaction conditions we provided, for which this conclusion relies on our assumption that the mobility of the $Au_{2057\pm45}$ monomer is responsible for the formation of dimers and trimers, while the formation of the

tetramer would arise largely due to the mobility of the dimer through two-body collisions.

In conclusion, the evolution of the sizes and atomic structures of mass-selected $Au_{561\pm13}$, $Au_{923\pm20}$, and $Au_{2057\pm45}$ clusters were investigated, both before and after being subjected to realistic catalytic CO combustion conditions. $Au_{561\pm13}$ and $Au_{923\pm20}$ were found to undergo Ostwald ripening, whereas for $Au_{2057\pm45}$, Smoluchowski ripening was observed instead. We suggest that the emergence of a crossover in ripening modes occurs due to the inability of the energy provided by the CO oxidation reaction to reach the activation threshold for Ostwald ripening for the largest mass-selected cluster size examined here.

■ EXPERIMENTAL SECTION

Gold nanoclusters were produced with a magnetron-sputtering gas-condensation cluster beam source.[69] An inline lateral time-of-flight mass filter is used to select clusters of a specific size, offering a mass resolution of $M/\Delta M \approx 23$ based on calibration with Ar^+. The mass-selected gold clusters are focused into the deposition chamber under high vacuum conditions ($10^{-7}–10^{-6}$ mbar), with each size deposited onto separate amorphous carbon films suspended on molybdenum TEM grids at a soft landing energy of 0.5 eV/atom. In this approach, Au clusters with 561 ± 13, 923 ± 20, and 2057 ± 45 were soft landed on the substrate.[46] Related cluster generation parameters: condensation length, 250 mm; magnetron sputtering power, 10 W DC; condensation gas flow rates, 200 sccm (Ar) and 150 sccm (He); condensation pressures, 2.05, 0.77, 0.86 mbar for Au_{561}, Au_{923}, Au_{2057}, respectively. After deposition, the Au clusters were imaged in HAADF-STEM, exposed to treatment conditions, and then imaged again. Samples were stored in a vacuum desiccator between measurements. The total time for which the Au clusters were exposed to atmospheric conditions during transfer between storage and instruments was <30 min. We find that, prior to treatment, the clusters maintained their high selective mass while stored in a vacuum desiccator at room temperature. Gas-phase reactions and treatments were conducted as previously reported.[70] Each TEM grid that carries Au clusters sits on a quartz wool plug in the middle of a quartz tube (length 360 mm, inner diameter 4 mm). For all treatments, the temperature was increased at a rate of 2 °C min^{-1} from room temperature to 250 °C and held at 250 °C for 2 h. For thermal treatment, pure He gas was used at an initial pressure of 0.32 bar, rising to 0.35 bar at 250 °C. For treatment with O_2, a mixture of 20.9% O_2 + 79.1% He was used, with the pressure initially at 0.10 bar rising to 0.14 bar ($Au_{923\pm20}$) and 0.12 bar ($Au_{2057\pm45}$) at 250 °C. For the full CO oxidation reaction, premixed CO and O_2 gases were diluted in pure He, resulting in a mixture of 1% CO + 20.9% O_2 + 78.1% He. The pressure was initially 0.11 bar (ambient temp.), rising to 0.15 and 0.1 bar (250 °C). After the temperature ramp cycle, pure He at room temperature was used to cool down the system for 15 min. Atomic resolution imaging was conducted with a JEOL 2100F STEM equipped with a spherical aberration probe corrector (CEOS GmbH) at a convergence angle of 20 mrad and a high-angle annular dark field (HAADF) detector. The microscope operates at 200 kV and the collecting angle on the HAADF detector is between 62 mrad (inner) and 164 mrad (outer). In total, 4025 nanoclusters were imaged at atomic resolution (6 Mx magnification or higher) in order to measure diameters from the images and assign the atomic structures. Additionally, a total of 3162 clusters were imaged at 2 Mx for measurement of the integrated HAADF intensities. In order to be able to assign the atomic structure for each cluster imaged, multislice HAADF-STEM image simulations were generated for Au_{561} and Au_{2057} using the QSTEM package. The previously published simulation atlas was used in the case of Au_{923}. This atlas covers a full range of possible orientations for a given high-symmetry structure. The simulation atlases for Au_{561} and Au_{2057} are provided in the Supporting Information. By comparing experimental images with image simulations atlases, the structure of each cluster can be assigned. In the image simulations, the following parameters were

used: spherical aberration $C_S = 1 \mu m$; defocus $C_1 = -19$ Å; acceleration voltage, probe convergence angle, and inner and outer collecting angles on HAADF detector are as described earlier.

■ ASSOCIATED CONTENT

Ⓢ Supporting Information

The Supporting Information is available free of charge on the ACS Publications website at DOI: 10.1021/jacs.5b08720.

> Simulation atlases for Au_{561} and Au_{2057} and figures showing the resilience of clusters under the electron beam. (PDF)

■ AUTHOR INFORMATION

Corresponding Author

*R.E.Palmer@bham.ac.uk

Notes

The authors declare no competing financial interest.

■ ACKNOWLEDGMENTS

■ REFERENCES

(1) Hansen, T.; Delariva, A.; Challa, S.; Datye, A. *Acc. Chem. Res.* **2013**, *46*, 1720−1730.

(2) Cao, A.; Lu, R.; Veser, G. *Phys. Chem. Chem. Phys.* **2010**, *12*, 13499−13510.

(3) Bartholomew, C. H. *Appl. Catal., A* **2001**, *212*, 17−60.

(4) Lopez-Acevedo, O.; Kacprzak, K. A.; Akola, J.; Häkkinen, H. *Nat. Chem.* **2010**, *2*, 329−334.

(5) Granqvist, C. G.; Buhrman, R. A. *J. Appl. Phys.* **1976**, *47*, 2200−2219.

(6) Wynblatt, P.; Gjostein, N. *Prog. Solid State Chem.* **1975**, *9*, 21−58.

(7) Granqvist, C. G.; Buhrman, R. a. *J. Catal.* **1976**, *42*, 477−479.

(8) Simonsen, S. B.; Chorkendorff, I.; Dahl, S.; Skoglundh, M.; Sehested, J.; Helveg, S. *J. Catal.* **2011**, *281*, 147−155.

(9) Simonsen, S. B.; Chorkendorff, I.; Dahl, S.; Skoglundh, M.; Sehested, J.; Helveg, S. *J. Am. Chem. Soc.* **2010**, *132*, 7968−7975.

(10) Challa, S. R.; Delariva, A. T.; Hansen, T. W.; Helveg, S.; Sehested, J.; Hansen, P. L.; Garzon, F.; Datye, A. K. *J. Am. Chem. Soc.* **2011**, *133*, 20672−20675.

(11) Uchiyama, T.; Yoshida, H.; Kuwauchi, Y.; Ichikawa, S.; Shimada, S.; Haruta, M.; Takeda, S. *Angew. Chem., Int. Ed.* **2011**, *50*, 10157−10160.

(12) Azubel, M.; Koivisto, J.; Malola, S.; Bushnell, D.; Hura, G.; Koh, A.; Tsunoyama, H.; Tsukuda, T.; Pettersson, M.; Häkkinen, H.; Kornberg, R. *Science* **2014**, *345*, 909−912.

(13) Hamilton, J.; Baetzold, R. *Science* **1979**, *205*, 1213−1220.

(14) Wettergren, K.; Schweinberger, F. F.; Deiana, D.; Ridge, C. J.; Crampton, A. S.; Ro, M. D.; Hansen, T. W.; Zhdanov, V. P.; Heiz, U.; Langhammer, C. *Nano Lett.* **2014**, *14*, 5803−5809.

(15) Campbell, C.; Parker, S.; Starr, D. *Science* **2002**, *298*, 811−814.

(16) Meyer, R.; Lemire, C.; Shaikhutdinov, S. K.; Freund, H. J. *Gold Bull.* **2004**, *37*, 72−124.

(17) Haruta, M. *J. Catal.* **1993**, *144*, 175−192.

(18) Haruta, M. *Catal. Today* **1997**, *861*, 153.

(19) Valden, M.; Lai, X.; Goodman, D. *Science* **1998**, *281*, 1647−1650.

(20) Lopez, N.; Janssens, T. V. W.; Clausen, B. S.; Xu, Y.; Mavrikakis, M.; Bligaard, T.; Nørskov, J. K. *J. Catal.* **2004**, *223*, 232−235.

(21) Comotti, M.; Li, W.-C.; Spliethoff, B.; Schüth, F. *J. Am. Chem. Soc.* **2006**, *128*, 917−924.

(22) Haruta, M. *Chem. Rec.* **2003**, *3*, 75−87.

(23) Sanchez, A.; Abbet, S.; Heiz, U.; Schneider, W.-D.; Häkkinen, H.; Barnett, R. N.; Landman, U. *J. Phys. Chem. A* **1999**, *103*, 9573−9578.

(24) Hashmi, A. S. K.; Hutchings, G. J. *Angew. Chem., Int. Ed.* **2006**, *45*, 7896−7936.

(25) Hutchings, G. J.; Carrettin, S.; Landon, P.; Edwards, J. K.; Enache, D.; Knight, D. W.; Xu, Y.-J.; Carley, A. F. *Top. Catal.* **2006**, *38*, 223−230.

(26) Bulushev, D. A.; Yuranov, I.; Suvorova, E. I.; Buffat, P. A.; Kiwi-Minsker, L. *J. Catal.* **2004**, *224*, 8−17.

(27) Akita, T.; Tanaka, K.; Kohyama, M.; Haruta, M. *Surf. Interface Anal.* **2008**, *40*, 1760−1763.

(28) Han, Y.; Ferrando, R.; Li, Z. Y. *J. Phys. Chem. Lett.* **2014**, *5*, 131−137.

(29) Larsen, A. H.; Kleis, J.; Thygesen, K. S.; Nørskov, J. K.; Jacobsen, K. W. *Phys. Rev. B: Condens. Matter Mater. Phys.* **2011**, *84*, 245429.

(30) Kleis, J.; Greeley, J.; Romero, N. A.; Morozov, V. A.; Falsig, H.; Larsen, A. H.; Lu, J.; Mortensen, J. J.; Dułak, M.; Thygesen, K. S.; Nørskov, J. K.; Jacobsen, K. W. *Catal. Lett.* **2011**, *141*, 1067−1071.

(31) Lopez, N.; Nørskov, J. K. *J. Am. Chem. Soc.* **2002**, *124*, 11262−11263. PMID: 12236728.

(32) Falsig, H.; Hvolbæk, B.; Kristensen, I. S.; Jiang, T.; Bligaard, T.; Christensen, C. H.; Nørskov, J. K. *Angew. Chem., Int. Ed.* **2008**, *47*, 4835−4839.

(33) Lopez, N.; Nørskov, J. K. *J. Am. Chem. Soc.* **2002**, *124*, 11262−11263.

(34) Herzing, A. A.; Kiely, C. J.; Carley, A. F.; Landon, P.; Hutchings, G. J. *Science* **2008**, *321*, 1331−1335.

(35) Yang, F.; Chen, M.; Goodman, D. *J. Phys. Chem. C* **2008**, *2*, 254−260.

(36) Li, H.; Li, L.; Pedersen, A.; Gao, Y.; Khetrapal, N.; Jónsson, H.; Zeng, X. C. *Nano Lett.* **2015**, *15*, 682−688.

(37) Plant, S. R.; Cao, L.; Palmer, R. E. *J. Am. Chem. Soc.* **2014**, *136*, 7559−7562.

(38) Fukamori, Y.; König, M.; Yoon, B.; Wang, B.; Esch, F.; Heiz, U.; Landman, U. *ChemCatChem* **2013**, *5*, 3330−3341.

(39) Mason, M. *Phys. Rev. B: Condens. Matter Mater. Phys.* **1983**, *27*, 748−762.

(40) Pauwels, B.; Van Tendeloo, G.; Bouwen, W.; Theil Kuhn, L.; Lievens, P.; Lei, H.; Hou, M. *Phys. Rev. B: Condens. Matter Mater. Phys.* **2000**, *62*, 10383−10393.

(41) Thune, E.; Carpene, E.; Sauthoff, K.; Seibt, M.; Reinke, P. *J. Appl. Phys.* **2005**, *98*, 034304.

(42) Plant, S. R.; Cao, L.; Yin, F.; Wang, Z. W.; Palmer, R. E. *Nanoscale* **2014**, *6*, 1258−1263.

(43) Arkill, K. P.; Mantell, J. M.; Plant, S. R.; Verkade, P.; Palmer, R. E. *Sci. Rep.* **2015**, *5*, 9234.

(44) Goldby, I.; Kuipers, L.; Von Issendorff, B.; Palmer, R. *Appl. Phys. Lett.* **1996**, *69*, 2819−2821.

(45) Carroll, S. J.; Palmer, R. E.; Mulheran, P. A.; Hobday, S.; Smith, R. *Appl. Phys. A: Mater. Sci. Process.* **1998**, *67*, 613−619.

(46) Carroll, S. J.; Weibel, P.; Von Issendorff, B.; Kuipers, L.; Palmer, R. E. *J. Phys.: Condens. Matter* **1996**, *8*, L617−L624.

(47) Carroll, S. J.; Pratontep, S.; Streun, M.; Palmer, R. E.; Hobday, S.; Smith, R. *J. Chem. Phys.* **2000**, *113*, 7723−7727.

(48) Yin, F.; Xirouchaki, C.; Guo, Q.; Palmer, R. E. *Adv. Mater.* **2005**, *17*, 731−734.

(49) Yin, F.; Lee, S.; Abdela, A.; Vajda, S.; Palmer, R. E. *J. Chem. Phys.* **2011**, *134*, 141101.

(50) Wang, Z. W.; Palmer, R. E. *Journal of Physics: Conference Series* **2012**, *371*, 012010.

(51) Valden, M.; Pak, S.; Lai, X.; Goodman, D. *Catal. Lett.* **1998**, *56*, 7−10.

(52) Liu, Z.-P.; Gong, X.-Q.; Kohanoff, J.; Sanchez, C.; Hu, P. *Phys. Rev. Lett.* **2003**, *91*, 266102.

(53) Ji, X.; Zuppero, A.; Gidwani, J. M.; Somorjai, G. A. *J. Am. Chem. Soc.* **2005**, *127*, 5792−5793.

(54) Ji, X. Z.; Somorjai, G. A. *J. Phys. Chem. B* **2005**, *109*, 22530−22535.

(55) Ji, X.; Zuppero, A.; Gidwani, J. M.; Somorjai, G. A. *Nano Lett.* **2005**, *5*, 753−756.

(56) Willneff, E. A.; Kiannerd, C.; Schroeder, S. L. M. *Chem. Commun.* **2003**, 258−259.

(57) Arenz, M.; Landman, U.; Heiz, U. *ChemPhysChem* **2006**, *7*, 1871−1879.

(58) Ouyang, R.; Liu, J. X.; Li, W. X. *J. Am. Chem. Soc.* **2013**, *135*, 1760−1771.

(59) Li, Z.; Young, N. P.; Di Vece, M.; Palomba, S.; Palmer, R. E.; Bleloch, A. L.; Curley, B. C.; Johnston, R. L.; Jiang, J.; Yuan, J. *Nature* **2008**, *451*, 46−48.

(60) Wang, Z. W.; Palmer, R. E. *Phys. Rev. Lett.* **2012**, DOI: 10.1103/PhysRevLett.108.245502.

(61) Wang, Z. W.; Palmer, R. E. *Nano Lett.* **2012**, *12*, 91−95.

(62) Wells, D. M.; Rossi, G.; Ferrando, R.; Palmer, R. E. *Nanoscale* **2015**, *7*, 6498−6503.

(63) Curley, B. C.; Johnston, R. L.; B, B.; Young, N. P.; Li, Z.; Vece, M. D.; Palmer, R. E.; Bleloch, A. *Methodology* **2007**, 1−12.

(64) Xiong, S.; Qi, W.; Cheng, Y.; Huang, B.; Wang, M.; Li, Y. *Phys. Chem. Chem. Phys.* **2011**, *13*, 10648−10651.

(65) Liu, D.; Lian, J. S.; Jiang, Q. *J. Phys. Chem. C* **2009**, *113*, 1168−1170.

(66) Baletto, F.; Ferrando, R.; Fortunelli, A.; Montalenti, F.; Mottet, C. *J. Chem. Phys.* **2002**, *116*, 3856.

(67) Mottet, C.; Goniakowski, J.; Baletto, F.; Ferrando, R.; Treglia, G. *Phase Transitions* **2004**, *77*, 101−113.

(68) Nanda, K. K. *Appl. Phys. Lett.* **2005**, *87*, 3−6.

(69) Pratontep, S.; Carroll, S. J.; Xirouchaki, C.; Streun, M.; Palmer, R. E. *Rev. Sci. Instrum.* **2005**, *76*, 045103.

(70) Hu, K.-J.; Plant, S. R.; Ellis, P. R.; Brown, C. M.; Bishop, P. T.; Palmer, R. E. *Phys. Chem. Chem. Phys.* **2014**, *16*, 26631−26637.